PCCP

PAPER

View Article Online
View Journal | View Issue

Cite this: *Phys. Chem. Chem. Phys.*, 2024, **26**, 4533

Full control of the orientation of non-symmetric molecules using weak and moderate electric fields

Rosario González-Férez [a] and Juan J. Omiste *[b]

Received 17th November 2023,
Accepted 8th January 2024

DOI: 10.1039/d3cp05592b

rsc.li/pccp

We investigate the full control over the orientation of a planar non-symmetric molecule by using moderate and weak electric fields. Quantum optimal control techniques allow us to orient any axis of 6-chloropyridazine-3-carbonitrile, which is taken as prototype example here, along the electric field direction. We perform a detailed analysis by exploring the impact on the molecular orientation of the time scale and strength of the control field. The underlying physical phenomena allowing for the control of the orientation are interpreted in terms of the frequencies contributing to the field-dressed dynamics and to the driving field by a spectral analysis.

1 Introduction

The interaction of external fields with molecules creates coherent superpositions of field-free rotational states[1,2] with plethora of applications in a wide range of areas from stereodynamics,[3–5] high precision measurements[6] and quantum information processing.[7,8] This interaction allows for the creation and control of highly rotating molecular states, namely superrotors,[9–11] the manipulation[12–15] and separation[16,17] of chiral molecules, the orientation of proteins,[18,19] the isotopic separation,[20] and the controlled manipulation of enantiomers of chiral molecules.[21]

The orientation of a molecule requires the angular confinement of a molecule-fixed axis along a laboratory-fixed one and a preferred direction of the electric dipole moment.[22–24] For asymmetric molecules, the 3D orientation implies that the all three molecular axes of inertia are confined to laboratory fixed ones and a well defined direction of the electric dipole moment.[25,26] Certain complex molecular systems, such as the planar molecule 6-chloropyridazine-3-carbonitrile and the chiral one bromochlorofluoromethane (CHBrClF), possess a permanent dipole moment which does not coincide with any inertia axis. For these systems, it may be necessary to control the orientation of a specific molecular axis different from the one defined by the electric dipole moment. Therefore, it is mandatory to design an specific protocol beyond brute force orientation[27] or standard mixed-field orientation[22,24] to accurately restrict the position of a given axis, *i.e.*, a given atom. Such a task could benefit from long-established algorithms, as the quantum optimal control (QOC)[28] to accurately drive the molecular dynamics, which is one of the most relevant and promising quantum control algorithms in many active areas of research.[29,30]

The fundamental concept of QOC involves designing a driving field that optimizes a certain expectation value or a state population in a quantum system. This is done by solving a self-consistent set of equations, for which several algorithms have been developed.[31,32] QOC constitutes a powerful tool for manipulating the dynamics of quantum systems,[28,32,33] including the control of qubits,[34] population of vibrational states,[35] and coupled spin dynamics,[36] among others. Regarding molecular orientation control, the Krotov algorithm[31,37,38] is used to design terahertz laser pulses,[39] or to manipulate the permanent dipole orientation of molecular ensembles, as reported in various studies.[40–43] In addition, this algorithm has been used to optimize alignment of molecules immersed in a thermal bath.[44,45]

In this work, we consider a non-symmetric molecule, and apply the QOC algorithm to optimize the orientation along several molecular directions. Nevertheless, this methodology may be applied to any molecular axis contained in the molecular plane. Our study provides physical insights into the design of driving fields for this purpose. In particular, we provide a deeper understanding of the mechanisms underlying the control by means of a spectral analysis of the field-dressed wavepacket and of the driving field. This paper is organized as follows. Section 2 provides the Hamiltonian in an electric field, and a brief overview of the QOC theory with the corresponding equations of motion. In Section 3, we present the QOC results for the planar molecule 6-chloropyridazine-3-carbonitrile (CPC), taken here as a prototype example, orienting its permanent dipole moment and principal axes of inertia within the molecular plane, while varying the control field strength and duration. Finally, Section 4 summarizes the main findings of the study and presents a short outlook.

[a] *Instituto Carlos I de Física Teórica y Computacional and Departamento de Física Atómica, Molecular y Nuclear, Universidad de Granada, 18071 Granada, Spain*
[b] *Departamento de Química Física, Universidad Complutense de Madrid, 28040 Madrid, Spain. E-mail: jomiste@ucm.es*

2 Theory and methods

2.1 The Hamiltonian

In this work we investigate the orientation of a planar molecule without rotational symmetry by means of an external time-dependent electric field $\vec{E}(t)$, which is taken parallel to the Laboratory Fixed Frame (LFF) Z-axis. We work within the Born–Oppenheimer and the rigid rotor approximation; therefore, the molecular system is described by the Hamiltonian:

$$H(t) = H_{\mathrm{rot}} + H_{\mathrm{E}}(t), \tag{1}$$

where $H_{\mathrm{rot}} = B_x J_x^2 + B_y J_y^2 + B_z J_z^2$ is the field-free Hamiltonian, J_k the projection of the angular momentum operator $\vec{J}$ along the k axis of the molecular fixed frame (MFF). The field-free rotational states are denoted by $J_{K_a,K_c}M$,[46] where J is the total angular momentum number and M the magnetic quantum number, *i.e.*, the projection of $\vec{J}$ along the LFF Z-axis, and K_a and K_c are the projection of $\vec{J}$ along the MFF z-axis in the prolate and oblate limiting cases, respectively.

The coupling of the molecular electric dipole moment $\vec{\mu}$ with an electric field parallel to the LFF Z-axis[27,47] reads

$$\begin{aligned} H_{\mathrm{E}}(t) &= -\vec{\mu}\cdot\vec{E}(t) = -E(t)\mu\cos\theta_{Z\mu} \\ &= -E(t)(\mu_z\cos\theta_{Zz} + \mu_x\cos\theta_{Zx}) \end{aligned} \tag{2}$$

with $\theta_{Z\mu}$ being the angle between $\vec{\mu}$ and the LFF Z-axis, and θ_{Zk} the Euler angle between the molecular k axis and LFF Z-axis.[48] The effect of this interaction is to orient the electric dipole moment along the electric field direction, which we characterize by $\langle\cos\theta_{Z\mu}\rangle$, in this work, we also explore the orientation of the MFF z and x axes along this LFF Z-axis in terms of $\langle\cos\theta_{Zz}\rangle$ and $\langle\cos\theta_{Zx}\rangle$, respectively.

2.2 Quantum optimal control

The goal of this work is to optimize the orientation of any molecular axis of an asymmetric planar molecule by using the quantum optimal control (QOC) methodology to design a time-dependent electric field while imposing certain restrictions. To do so, we define the following functional[31]

$$\mathscr{J}(\chi,\psi,E,\alpha) = \mathscr{J}_{\mathrm{S}}(\chi,E,\psi) + \mathscr{J}_{\mathrm{p}}(E,\alpha) + \mathscr{J}_{\mathrm{o}}(\psi) \tag{3}$$

and seek for stationary trajectories in the system variables, *i.e.*, the driving field $E(t)$ and the wavefunction $\psi(t)$.† The first term in $\mathscr{J}(\chi,\psi,E,\alpha)$, guarantees that the time-dependent Schrödinger equation is fulfilled by introducing the Lagrange multiplier $\chi(t)$:

$$J_{\mathrm{S}}(\chi,E,\psi) = -2\mathrm{Im}\left[\int_{T_0}^{T}\mathrm{d}t\langle\chi(t)|i\partial_t - H(t)|\psi(t)\rangle\right], \tag{4}$$

where Im denotes the imaginary part, and T_0 and T are the initial propagation time and the measuring time, respectively.

† Note that we omit any spatial dependency in the functions for the sake of clarity.

The penalty functional $\mathscr{J}_{\mathrm{p}}(E,\alpha)$ reads as

$$\mathscr{J}_{\mathrm{p}}(E,\alpha) = -\alpha\int_{T_0}^{T}\mathrm{d}t\frac{E(t)^2}{S(t)}, \tag{5}$$

and forces a low fluence of the field by tuning the mask function $S(t)$ and a penalty factor α. The last term $\mathscr{J}_{\mathrm{o}}(\psi)$ maximizes the expectation value of the operator O at the final time $t = T$:

$$\mathscr{J}_{\mathrm{o}}(\psi) = \langle\psi(T)|O|\psi(T)\rangle. \tag{6}$$

Note that the stationary trajectory fulfils $\mathscr{J}_{\mathrm{S}}(\chi,E,\psi) = 0$ and maximizes (minimizes) $\mathscr{J}_{\mathrm{p}}(E,\alpha) + \mathscr{J}_{\mathrm{o}}(\psi)$. To achieve the latter, the values of α and the function $S(t)$ must be carefully chosen such that the contribution of the fluence of $E(t)$ is small compared to $\langle O\rangle$.

The QOC equations[31] are obtained by solving the Euler equation associated with the functional $\mathscr{J}(\chi,\psi,E,\alpha)$ eqn (3) and are given by

$$i\partial_t\psi(t) - H(t)\psi(t) = 0, \tag{7}$$

$$i\partial_t\chi(t) - H(t)\chi(t) = 0, \tag{8}$$

$$\chi(T) = O\psi(T), \tag{9}$$

$$\vec{E}(t) = -\frac{S(t)}{\alpha}\mathrm{Im}[\langle\chi(t)|\vec{\mu}|\psi(t)\rangle], \tag{10}$$

and their complex conjugates. This self-consistent system of equations is solved using the Krotov method,[31,37,38] which converges to a stationary solution for positive defined observable operators.[49] Hence, to maximize the orientation $\langle\cos\theta_{Zk}\rangle$ and to ensure the convergence of the algorithm, we set $O = \cos\theta_{Zk} + 1$. Let us remark that by maximizing the orientation we also ensure a high degree of alignment, since $\langle\cos^2\theta_{Zk}\rangle \geq \langle\cos\theta_{Zk}\rangle^2$.

In order to describe the dynamics, we solve the time dependent Schrödinger equation associated with the Hamiltonian in eqn (1). A basis set expansion of the wavefunction $\Psi(\Omega,t)$ is done in terms of the Wigner matrix elements,[48] and their most relevant properties and the matrix elements required are given in detailed elsewhere.[48] In this basis expansion, we take into account that magnetic quantum number M is conserved, because the electric field $\vec{E}(t)$ is parallel to the LFF Z-axis. For the time propagation, we apply the short iterative Lanczos scheme.[50]

3 Results

As an example of non-symmetric planar molecules, we use 6-chloropyridazine-3-carbonitrile, with rotational constants B_x = 717.42 MHz, B_y = 639.71 MHz and B_z = 5905 MHz.[51] This molecule is characterized by having its electric dipole moment not parallel to any principal axis of inertia, as shown in Fig. 1, with μ = 5.20 D and components μ_x = 4.37 D and μ_z = 2.83 D.[51] We focus on the field-dressed dynamics of the rotational ground state. To provide a deeper physical insight into the QOC mechanism, we explore the orientation along the driving field direction of the permanent dipole moment, $\vec{\mu}$, and the

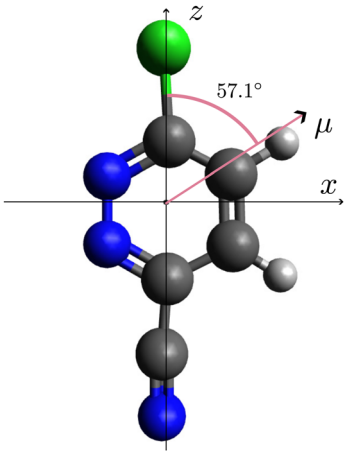

Fig. 1 Sketch of the molecular structure of 6-chloropyridazine-3-carbonitrile (CPC). The molecular geometry and the dipole moment, $\vec{\mu}$, are taken from ref. 51.

Table 1 Transition frequencies between the main rotational states involved in the field-dressed dynamics

Transition	Frequency (GHz)	Transition	Frequency (GHz)
$0_{00}0 \leftrightarrow 1_{01}0$	1.35	$4_{04}0 \leftrightarrow 5_{05}0$	6.76
$1_{10}0 \leftrightarrow 2_{02}0$	2.47	$1_{01}0 \leftrightarrow 2_{11}0$	7.81
$1_{10}0 \leftrightarrow 2_{11}0$	2.63	$2_{02}0 \leftrightarrow 3_{12}0$	9.05
$1_{01}0 \leftrightarrow 2_{02}0$	2.71	$2_{20}0 \leftrightarrow 3_{12}0$	11.87
$2_{02}0 \leftrightarrow 3_{03}0$	4.06	$8_{08}0 \leftrightarrow 9_{18}0$	15.84
$3_{03}0 \leftrightarrow 4_{04}0$	5.41	$1_{10}0 \leftrightarrow 2_{20}0$	18.40
$0_{00}0 \leftrightarrow 1_{10}0$	6.53	$2_{20}0 \leftrightarrow 3_{30}0$	30.27

principal axes of inertia in the molecular plane x and z. Note that the orientation may be maximized along any direction in the molecular plane.

For the mask function of the electric field, we use a Gaussian envelope $S(t) = \exp\left(-\frac{4t^2 \ln 2}{\tau^2}\right)$, with τ being the Full Width at Half Maximum (FWHM). The time interval is set to $[T_0,T] = [-2.53\tau,2.53\tau]$, taking $T = -T_0 = \sqrt{\frac{\ln 5 \times 10^7}{\ln 2}}\frac{\tau}{2}$ for computational convenience. The field-dressed dynamics is analyzed in terms of transition between field-free rotational states involved in the optimal control process. The most relevant transitions and their frequencies are collected in Table 1. These frequencies also allow us to interpret the structure of the driving field in the forthcoming sections.

3.1 Quantum optimal control for the fixed penalty parameter α

In this section, we set $\alpha = 10^6$ for the driving electric field, which is equivalent to fixing its maximum allowed strength given by μ/α, and consider two different FWHMs τ. For a 1 ns-FWHM field, the results obtained when the expectation value $\langle\cos\theta_{Zz}\rangle$ is optimized are presented in Fig. 2(a)–(d). The driving field designs a wavepacket populating rotational states and adjusting their relative phases. The time-evolution of the quantum interferences between these populated states provokes that $\langle\cos\theta_{Zz}\rangle$ reaches a maximum at the final T as shown in Fig. 2(a). During the time-evolution, the orientation varies between $\langle\cos\theta_{Zz}\rangle = -0.48$ and $\langle\cos\theta_{Zz}\rangle = 0.824$, and its oscillation pattern indicates that only a few states are involved in the dynamics. A spectral analysis of $\langle\cos\theta_{Zz}\rangle$ encounters three main frequencies 1.38, 2.77 and 4.15 GHz, associated with the transitions $0_{00}0 \leftrightarrow 1_{01}0$, $1_{01}0 \leftrightarrow 2_{02}0$ and $2_{02}0 \leftrightarrow 3_{03}0$, respectively, see Table 1. These rotational states are linked by the selection rules $\Delta J = \pm 1$ and $\Delta M = 0$, imposed by the operator $\cos\theta_{Zz}$[48,52] in eqn (2). For this optimization, the driving electric field in Fig. 2(d) is mostly relevant before $t = 0$ finding two main peaks at $t = -0.56$ ns and $t = -0.35$ ns with intensity 0.87 kV cm^{-1} and -1 kV cm^{-1}, respectively, being very weak afterwards. This control field is also mainly formed by these transition frequencies, as illustrated by the square of its Fourier Transform $|\mathscr{F}[E(t)]|^2$ in Fig. 3. Note that $|\mathscr{F}[E(t)]|^2$ is normalized so its maximum value is 1. The wide peaks of the $\tau = 1$ ns

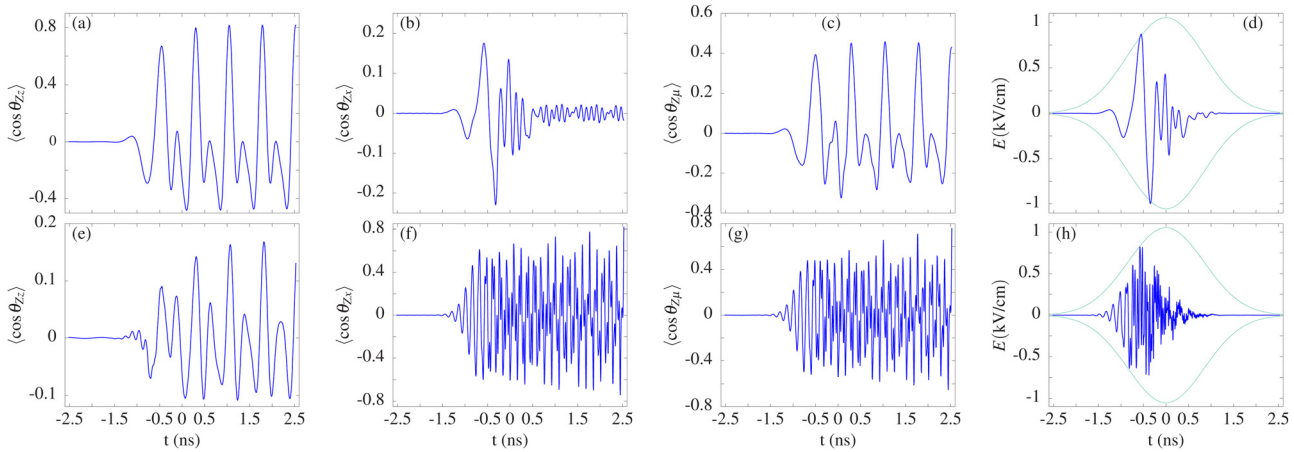

Fig. 2 Optimization of $\langle\cos\theta_{Zz}\rangle$ (panels (a)–(d) in the upper row) and $\langle\cos\theta_{Zx}\rangle$ (panels (e)–(h) in the lower row) for the initial state $0_{00}0$. (a) and (e) $\langle\cos\theta_{Zz}\rangle$; (b) and (f) $\langle\cos\theta_{Zx}\rangle$; (c) and (g) $\langle\cos\theta_{Z\mu}\rangle$; and (d) and (h) optimal electric field $E(t)$ and mask function $\pm\frac{S(t)}{\alpha}$ as a function of time. The parameters τ and α are set to 1 ns and 10^6, respectively.

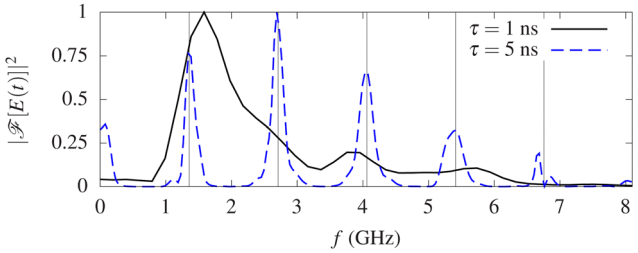

Fig. 3 For $\alpha = 10^6$ and FHWMs $\tau = 1$ and 5 ns, the absolute squared Fourier transform of the optimized electric field, $|\mathscr{F}[E(t)]|^2$ to maximize $\langle\cos\theta_{Zz}\rangle$. Note that $|\mathscr{F}[E(t)]|^2$ is normalized so that the absolute maximum equals 1.

field are due to the duration imposed in the optimization algorithm. One can distinguish the frequencies 1.35, 4.06 and 5.41 GHz, associated with the transitions $0_{00}0 \leftrightarrow 1_{01}0$, $2_{02}0 \leftrightarrow 3_{03}0$ and $3_{03}0 \leftrightarrow 4_{04}0$, respectively. Note that the contribution of the latter in the orientation pattern is negligible. The frequency 2.77 GHz from the $1_{01}0 \leftrightarrow 2_{02}0$ transition is blurred due to the overlap with the preceding peaks. Despite the field being designed to optimize $\langle\cos\theta_{Zz}\rangle$, we encounter a moderate orientation of the molecular x-axis in Fig. 2(c) due to the coupling through μ_x. The orientation $\langle\cos\theta_{Zx}\rangle$ faithfully follows the external field until $t \approx 0.5$ ns. From there on the field is very small, and $\langle\cos\theta_{Zx}\rangle$ oscillates with a small amplitude reaching $\langle\cos\theta_{Zx}\rangle = -0.028$ at $t = T$. Reaching this almost zero orientation is possible since the time scale required for the x-axis dynamics is shorter than the period of oscillation of the electric field. Hence the impact of the driving field averages out due to the rapid oscillation of the molecule. The frequency of the x axis orientation is determined by the rotational constants of the orthogonal axes, namely B_y and B_z, which have an average value of approximately 3.27 GHz. This frequency is greater than the oscillation frequency of the driving field, which is around 1.6 GHz. The spectral analysis of $\langle\cos\theta_{Zx}\rangle$ confirms that the states $1_{10}0$, $2_{11}0$ and $3_{12}0$ are also populated in the field-dressed dynamics. For the sake of completeness, we present $\langle\cos\theta_{Z\mu}\rangle$ in Fig. 2(c), which shows a similar behaviour to $\langle\cos\theta_{Zz}\rangle$.

The driving field and the dressed rotational dynamics are highly complex when the QOC technique is applied to the orientation of the molecular x-axis. In Fig. 2(f), $\langle\cos\theta_{Zx}\rangle$ shows a complex oscillatory behaviour, which is due to the different time scale associated with the dynamics along this axis. At $t = T$ a large orientation is reached $\langle\cos\theta_{Zx}\rangle \approx 0.83$. The driving field is presented in Fig. 2(h), $E(t)$ rapidly oscillates for $t \lesssim 0.5$ ns, which contrasts with the slow oscillations of field optimizing $\langle\cos\theta_{Zz}\rangle$ in Fig. 2(d). This behaviour agrees with the rapid rotational dynamics of the MFF x-axis indicated above, and $\langle\cos\theta_{Zx}\rangle$ follows the field oscillations in Fig. 2(f). The Fourier Transform of $\langle\cos\theta_{Zx}\rangle$ shows three main frequencies, namely, 6.45 GHz, 18.47 GHz and 30.40 GHz, associated with the transitions $0_{00}0 \leftrightarrow 1_{10}0$, $1_{10}0 \leftrightarrow 2_{20}0$ and $2_{20}0 \leftrightarrow 3_{30}0$, respectively. Now, the orientation of the dipole moment along the LFF Z-axis $\langle\cos\theta_{Z\mu}\rangle$, see Fig. 2(g) follows a similar behaviour to $\langle\cos\theta_{Zx}\rangle$, and a significant value is reached at $t = T$ with $\langle\cos\theta_{Z\mu}\rangle = 0.76$.

In contrast, $\langle\cos\theta_{Zz}\rangle$ is incapable of adjusting to the rapidly changing driving field as observed in Fig. 2(e). Indeed, the control field in Fig. 2(h) imprints short transfers of momentum at each cycle, similar to the impulsive alignment described for short laser pulses.[1] As a consequence, the amplitude of $\langle\cos\theta_{Zz}\rangle$ cannot be efficiently reduced at the final time in general. To bypass this effect, the algorithm fine tunes all the relative quantum phases within the wavepacket, seeking for reducing the orientation of the z-axis, *i.e.*, approaching it to zero, at the final time $t = T$. However, if the pulse duration is short compared to the time characteristic of the z-axis dynamics, the oscillation may not vanish. This is the case in Fig. 2(e), where the orientation of the molecular z-axis is not negligible, *i.e.*, $\langle\cos\theta_{Zz}\rangle \approx 0.16$, at $t = T$, which is due to the short FWHM, $\tau = 1$ ns, of the driving field.

We now consider an optimizing field with $\tau = 5$ ns FWHM and explore the results of the QOC algorithm applied to the three possible orientation axes. Compared to the 1 ns pulse in Fig. 2(a), $\langle\cos\theta_{Zz}\rangle$ exhibits faster oscillations with large amplitude, which increase up to the maximal value $\langle\cos\theta_{Zz}\rangle = 0.9$ at $t = T$. The optimized electric field, see Fig. 4(a), also possesses rapid oscillations mainly for $t \lesssim 0$ ns when the rotational wavepacket is created. In particular, for $t \lesssim -3.5$ ns, $\langle\cos\theta_{Zz}\rangle$ follows this driving field. The spectral analysis given by the Fourier Transform of the field in Fig. 3 presents clearly defined and well separated peaks. This larger FWHM allows the population of highly excited rotational states associated with the additional frequency 6.76 GHz of the $4_{04}0 \leftrightarrow 5_{05}0$ transition. Panels (b) and (c) of Fig. 4 present the orientation of the MFF x axis and $\vec{\mu}$ along the LFF Z-axis. As in the previous case, the behaviour of $\langle\cos\theta_{Z\mu}\rangle$ resembles $\langle\cos\theta_{Zz}\rangle$, but reaching smaller final value with $\langle\cos\theta_{Z\mu}\rangle = 0.502$ at $t = T$. In contrast, $\langle\cos\theta_{Zx}\rangle$ shows rapid oscillations of small amplitude for $t > 0$ ns, and at $t = T$ $\langle\cos\theta_{Zx}\rangle = 0.015$.

The results obtained when $\langle\cos\theta_{Zx}\rangle$ is optimized are shown in Fig. 4(e)–(h). The driving field in Fig. 4(h), presents a more complex structure with faster and narrower oscillations compared to the previous field in Fig. 4(d). The number of rotational states contributing to the field-dressed dynamics is enhanced, as it is manifested in the irregular oscillations of $\langle\cos\theta_{Zz}\rangle$, $\langle\cos\theta_{Zx}\rangle$ and $\langle\cos\theta_{Z\mu}\rangle$ in Fig. 4(e), (f) and (g), respectively. During the time evolution, $\langle\cos\theta_{Zz}\rangle$ shows moderate values, but the field is adjusted to reduce it at $t = T$ attaining $\langle\cos\theta_{Zz}\rangle \approx 0.019$. In contrast, the orientation of the MFF x-axis is significantly enhanced to $\langle\cos\theta_{Zx}\rangle \approx 0.92$ at $t = T$, and $\langle\cos\theta_{Z\mu}\rangle$ presents a similar behaviour.

For completeness, we present the optimization of the orientation of the dipole-moment axis in Fig. 4(i)–(l). In this case, the quantum interference is constructive for $\langle\cos\theta_{Zx}\rangle$ and $\langle\cos\theta_{Zz}\rangle$, having both a local maximum at $t = T$ $\langle\cos\theta_{Zz}\rangle \approx 0.50$ and $\langle\cos\theta_{Zx}\rangle \approx 0.77$, whereas $\langle\cos\theta_{Z\mu}\rangle \approx 0.92$. This illustrates that the orientation of the permanent dipole moment is largely dominated by its x component. The spectral analysis of $E(t)$ shows that the transitions collected in Table 1 are relevant for the QOC, *i.e.*, these rotational states build up the control dynamics and maximal orientation of $\vec{\mu}$.

3.2 Quantum optimal control for varying the penalty factor α

In this section, we investigate the QOC orientation for different values of α, *i.e.*, the maximum allowed strength of the control

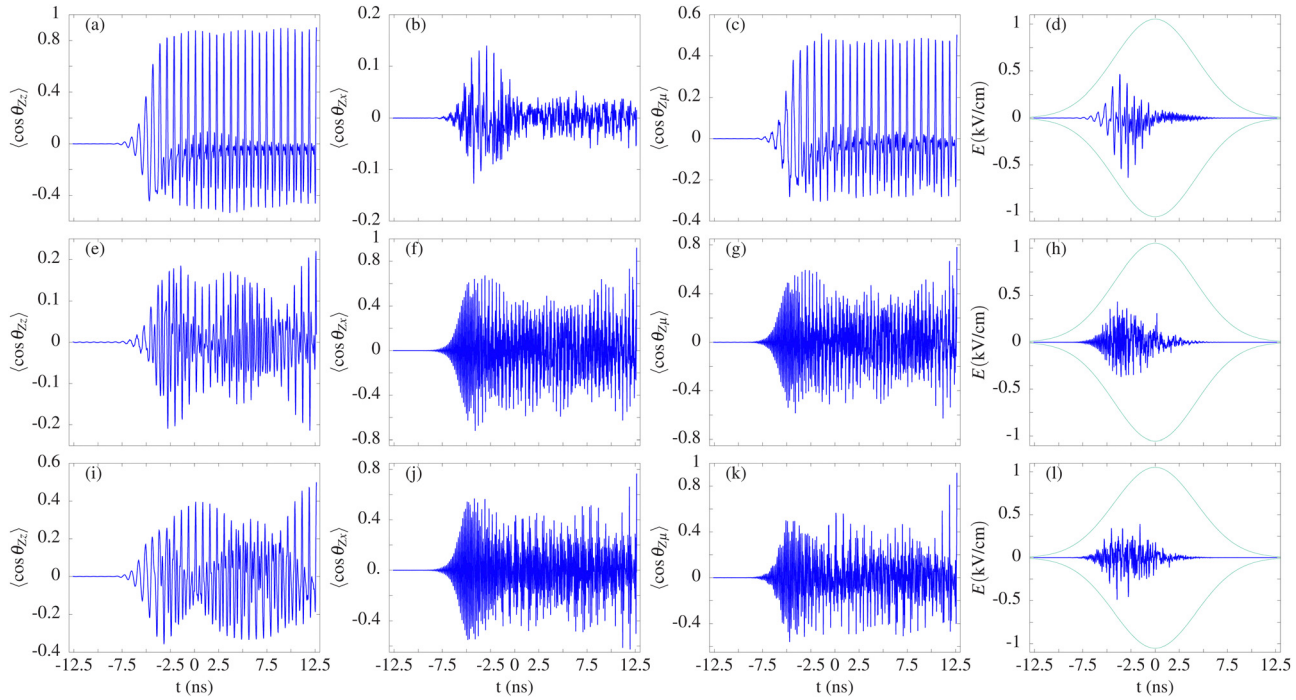

Fig. 4 Optimization of $\langle\cos\theta_{Zz}\rangle$ (panels (a)–(d) in the upper row) and $\langle\cos\theta_{Zx}\rangle$ (panels (e)–(h) in the middle row) and $\langle\cos\theta_{Z\mu}\rangle$ (panels (e)–(h) in the lower row) for the initial state $0_{00}0$. (a), (e) and (i): $\langle\cos\theta_{Zz}\rangle$; (b), (f) and (j): $\langle\cos\theta_{Zx}\rangle$; (c), (g) and (k): $\langle\cos\theta_{Z\mu}\rangle$; and (d), (h) and (l): optimal electric field $E(t)$ and mask function $\pm\frac{S(t)}{\alpha}$ as a function of time. The parameters τ and α are set to 5 ns and 10^6, respectively.

field, which is represented by the factor μ/α. For τ = 1 and 5 ns, we present in Fig. 5 the final optimized orientation as a function of the penalty factor α. Our analysis reveals that for a given α and τ, optimizing $\langle\cos\theta_{Zx}\rangle$ results in a larger orientation compared to $\langle\cos\theta_{Zz}\rangle$. This finding supports the idea that QOC is more effective when the natural timescale of the degree of freedom being optimized is smaller than the field duration, as discussed in Section 3.1. Moreover, for a given α, the larger the FWHM the better the optimized orientation is, for both $\langle\cos\theta_{Zx}\rangle$ and $\langle\cos\theta_{Zz}\rangle$.

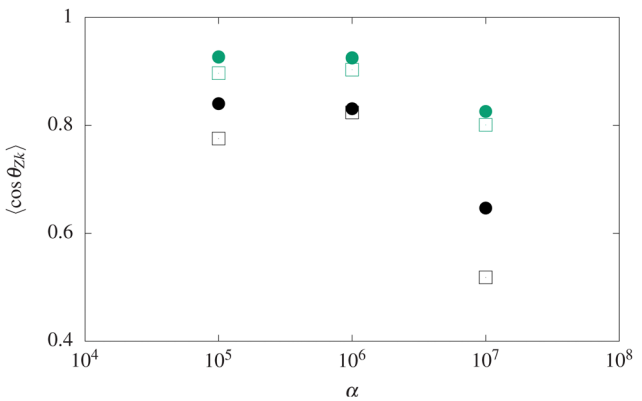

Fig. 5 Final orientations of the MFF x (bullets) and z (squares) axes, $\langle\cos\theta_{Zx}\rangle$ and $\langle\cos\theta_{Zz}\rangle$, respectively, after applying QOC using electric fields with FWHM τ = 1 (black) and 5 ns (green) as a function of the penalty factor α.

Our analysis also reveals that, for the values of α considered, $\langle\cos\theta_{Zx}\rangle$ decreases as a function of α, meaning that stronger fields result in larger optimized orientations. Note that for both FWHMs, $\langle\cos\theta_{Zx}\rangle$ is very similar for $\alpha = 10^5$ and 10^6, *i.e.*, the orientation saturates beyond certain intensities of the driving field. Since the orientation is not increasing, the functional $\mathcal{J}_o + \mathcal{J}_p$ is maximized by minimizing the fluence of the field, involved in the penalty functional, $\mathcal{J}_p$. This saturation of $\langle\cos\theta_{Zx}\rangle$ with α can be explained in terms of the brute force orientation occurring at these strong fields, combined with the larger frequencies along the MFF x-axis facilitating that the molecule follows the driving field. Furthermore, for $\alpha = 10^5$, that is, the stronger field case, the population transfer may not be understood in terms of one-photon transition, but as a strong field process.

In contrast, the orientation of the MFF z-axis decreases as α decreases, *i.e.*, as the maximal field strength increases. This is due to the strong dependence of the controllability of the orientation of this axis on the process for the suppression of $\langle\cos\theta_{Zx}\rangle$ imposed by the QOC equations. Note that the faster dynamics of the x axis and the larger component of $\vec{\mu}$ along x also play an important role against reducing $\langle\cos\theta_{Zx}\rangle$. Thus, achieving this suppression requires finely tuned quantum phases among the rotational states, as small changes can result in different outcomes. Besides, the QOC algorithm aims to maximize $\mathcal{J}_p(E,\alpha) + \mathcal{J}_o(\psi)$, as discussed in Section 2.2. However, due to the limited control of $\mathcal{J}_o(\psi)$, a better approach to the stationary point is reached for smaller $\mathcal{J}_o(\psi)$, and larger $\mathcal{J}_p(E,\alpha)$.

Finally, we perform a spectral analysis of the optimization along the x, z, and μ axes for the impact parameter $\alpha = 10^5$ and 10^7 and $\tau = 5$ ns. The Fourier transforms of the QOC fields are shown in Fig. 6, together with the frequencies of the main transitions between field-free rotational states, which are also collected in Table 1. In the weak field regime, $\alpha = 10^7$, shown in Fig. 6(a), we observe well-defined isolated frequencies for all the optimized orientation observables. The frequencies of $E(t)$ obtained from the optimization of $\langle\cos\theta_{Zz}\rangle$ and $\langle\cos\theta_{Zx}\rangle$ are different due to the different selection rules $\Delta K = 0$ and $\Delta K = \pm 1$ imposed by the operators μ_z and μ_x, respectively. For the initial state $0_{00}0$, the relevant transitions for the optimization of the z-axis orientation are $0_{00}0 \leftrightarrow 1_{01}0$, $1_{01}0 \leftrightarrow 2_{02}0$, and $2_{02}0 \leftrightarrow 3_{03}0$, which are characterized by frequencies of 1.35, 2.71, and 4.06 GHz, respectively. However, the optimization of $\langle\cos\theta_{Zx}\rangle$ is dominated by the frequencies mixing K, specifically $0_{00}0 \leftrightarrow 1_{10}0$ (6.53 GHz), $1_{10}0 \leftrightarrow 2_{02}0$ (2.47 GHz), $2_{02}0 \leftrightarrow 3_{12}0$ (9.05 GHz). The relatively low value of $\langle\cos\theta_{Zx}\rangle$ at $t = T$, see Fig. 5, can be explained in terms of the relevant frequencies in $E(t)$ for the orientation of $\langle\cos\theta_{Zz}\rangle$ being below the frequency required to transfer the population from $0_{00}0$ to $1_{10}0$, which is the first excited state coupled by μ_x. In contrast, the transition frequencies of $0_{00}0 \leftrightarrow 1_{10}0$ and $2_{02}0 \leftrightarrow 3_{12}0$ are above the main transitions. This results in the impulsive orientation of the molecular Z-axis as discussed in Section 3.1. Additional frequencies are observed in Fig. 6(a) when the orientation of the permanent dipole moment is optimized, with two new peaks at 2.63 and 7.81 GHz due to $1_{10}0 \leftrightarrow 2_{11}0$ and $1_{01}0 \leftrightarrow 2_{11}0$, respectively.

For a strong control field with $\alpha = 10^5$, the spectrum becomes more complex due to two main reasons. Firstly, the contribution of more excited rotational states, such as the peak at 15.84 GHz corresponding to the transition $8_{08}0 \leftrightarrow 9_{18}0$, which appears for the orientation of the MFF x-axis along the LFF Z-axis. Secondly, the brute force orientation mediated by the large amplitude of the field, as reported in previous studies.[22,27] Therefore, the driving field cannot be simply described as the contribution of several frequencies, *i.e.*, as population transfer mediated by absorption of several photons, due to the high intensity of the driving field, as we discussed in Section 3.2.

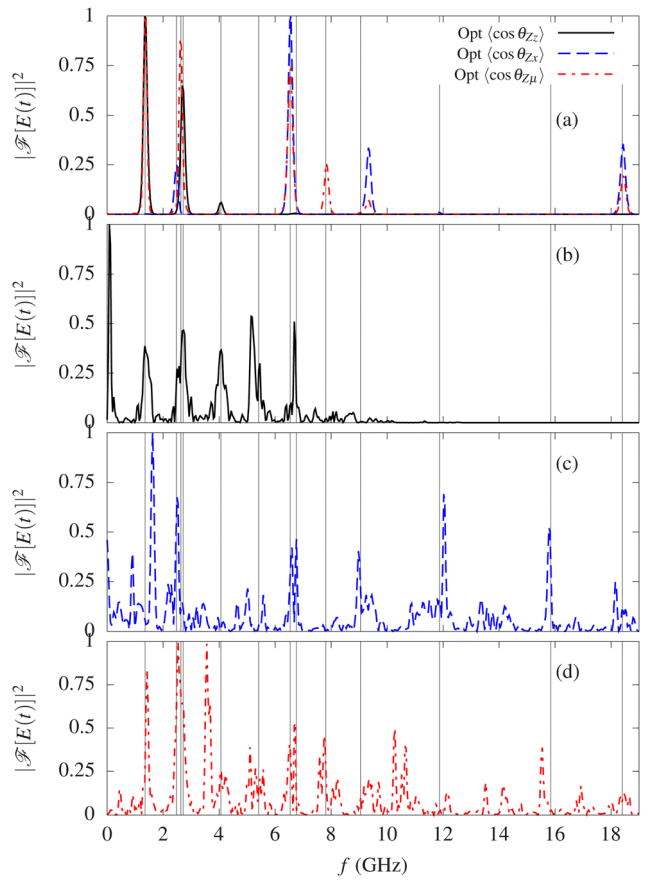

Fig. 6 For a pulse duration of $\tau = 5$ ns, the absolute squared Fourier transform, $|\mathscr{F}[E(t)]|^2$, of the optimized electric field is shown for (a) $\alpha = 10^7$ and (b)–(d) $\alpha = 10^5$. The Fourier transform plotted corresponds to optimization of $\langle\cos\theta_{Zz}\rangle$ (solid black), $\langle\cos\theta_{Zx}\rangle$ (blue dashed), and $\langle\cos\theta_{Z\mu}\rangle$ (red dot-dashed) and taking as initial state $0_{00}0$. The vertical lines correspond to the transition frequencies shown in Table 1. Note that $|\mathscr{F}[E(t)]|^2$ is normalized so that the absolute maximum equals 1.

4 Conclusions and outlook

In this work, we have demonstrated the feasibility of fully controlling the orientation of non-symmetric planar molecules along several axes, *i.e.*, the principal axes of inertia x and z and $\vec{\mu}$, by means of quantum optimal control. The driving field is composed of just a few frequencies corresponding to transitions among several field-free states, and its temporal profile and strength can be reached experimentally. For a mask function with FWHM and weak strength, our findings show limited control due to the small population transfer stimulated by the interaction with the field. In contrast, the electric field cannot be described by isolated components for strengths above 1 kV cm^{-1}, since the number of transitions among the involved states increases and they overlap due to their spectral width. This effect is further enhanced for short pulses. This work shows the efficiency, flexibility and potential of QOC for the rotational dynamics control of non-symmetric molecules and provides valuable physical insights into the conditions required for it. In addition, we have checked that the orientation may be maximize along any direction in the molecular plane.

Here, we focus on the stereodynamics of the ground state of CPC, and without loss of generality, the results could be extended to excited states. To tackle more realistic experimental conditions, and to face the difficulties of creating samples of ground-state molecules, we aim to generalize our study to thermal ensembles by means of the Von Neumann formalism. In this work, the QOC methodology has been applied to a near prolate molecule, but the main findings also hold for oblate molecules or any asymmetric top. Consequently, the frequencies of the driving field will vary according to the field-free spectrum of the considered molecular system. Furthermore, the rotational dynamics has been controlled by means of the orientation of a certain molecular axis, and analogous

procedure might be followed if such control is exerted in terms of the alignment.

Hence, this technique provides an alternative strategy to the mixed-field orientation method, which, in the case of CPC, was shown to attain full control of only one molecular axis.[51,53] Experimentally, it is still challenging to produce and control complex electric fields in the order of GHz. However, we have shown that only a limited number of frequencies are involved in the case of weak electric fields, simplifying the design and creation of these control fields, as it is the case of three-wave mixing experiments.[13] Indeed, for driving fields involving less frequencies, the control process is more robust. In addition, the optimal orientation is sensitive to the control field parameters, which might be subject to experimental errors. We have checked that small perturbations of the control field diminish this optimal orientation, but are still high, *i.e.*, reaching orientation values above 0.75.

Summing up, we have demonstrated that QOC is a powerful technique to control the orientation of any planar molecule without rotational symmetry, with a dipole moment not parallel to any molecular axis. We expect that our methodology is also efficient for the general molecular species, and it would be subject to further investigation. This class of molecules includes the enantiomers, whose manipulation, control and selection of chiral molecules[14,17,54,55] could have an enormous impact, for instance, on the pharmaceutical industry, where the spatial arrangement of the atoms in one enantiomer may determine the biological activity of a drug, as the remarkable case of thalidomide.[56] Moreover, creating optimally designed chiral electric fields could be used to efficiently create oriented superrotor states.[12]

Author contributions

J. J. O. proposed the research idea and formulated the theoretical framework. J. J. O. also developed the computational code for solving the Schrödinger equation and the Krotov algorithm and analyzed the results. R. G. F. and J. J. O. contributed equally to write the manuscript and to interpret the results.

Conflicts of interest

There are no conflicts to declare.

Acknowledgements

J. J. O. acknowledges the funding by the Madrid Government (Comunidad de Madrid Spain) under the Multiannual Agreement with Universidad Complutense de Madrid in the line Research Incentive for Young PhDs, in the context of the V PRICIT (Regional Programme of Research and Technological Innovation) (Grant: PR27/21-010), Projects PID2019-105458RB-I00 and PID2021-122839NB-I00 (MICIN). R. G. F. gratefully acknowledges financial support by the Spanish projects PID20 20-113390GB-I00 (MICIN), PY20-00082 (Junta de Andalucía), and A-FQM-52-UGR20 (ERDF-University of Granada) and the Andalusian research group FQM-207. We would also like to thank Ignacio Solá and Fernando Troyano for fruitful discussions.

Notes and references

1 H. Stapelfeldt and T. Seideman, *Rev. Mod. Phys.*, 2003, **75**, 543–557.
2 C. P. Koch, M. Lemeshko and D. Sugny, *Rev. Mod. Phys.*, 2019, **91**, 035005.
3 D. R. Herschbach, *Eur. Phys. J. D*, 2006, **38**, 3–13.
4 V. Aquilanti, M. Bartolomei, F. Pirani, D. Cappelletti and F. Vecchiocattivi, *Phys. Chem. Chem. Phys.*, 2005, **7**, 291–300.
5 D. Yang, D. Xie and H. Guo, *J. Phys. Chem. Lett.*, 2022, **2022**, 1777–1784.
6 I. Kozyryev and N. R. Hutzler, *Phys. Rev. Lett.*, 2017, **119**, 133002.
7 D. DeMille, *Phys. Rev. Lett.*, 2002, **88**, 067901.
8 V. V. Albert, J. P. Covey and J. Preskill, *Phys. Rev. X*, 2020, **10**, 031050.
9 A. Korobenko, A. A. Milner and V. Milner, *Phys. Rev. Lett.*, 2014, **112**, 113004.
10 A. Korobenko and V. Milner, *Phys. Rev. Lett.*, 2016, **116**, 183001.
11 A. A. Milner, A. Korobenko and V. Milner, *Phys. Rev. A*, 2016, **93**, 053408.
12 I. Tutunnikov, L. Xu, R. W. Field, K. A. Nelson, Y. Prior and I. S. Averbukh, *Phys. Rev. Res.*, 2021, **3**, 013249.
13 D. Patterson and J. M. Doyle, *Phys. Rev. Lett.*, 2013, **111**, 023008.
14 M. Leibscher, E. Pozzoli, C. Pérez, M. Schnell, M. Sigalotti, U. Boscain and C. P. Koch, *Commun. Phys.*, 2022, **5**, 110.
15 W. Sun, D. S. Tikhonov, H. Singh, A. L. Steber, C. Pérez and M. Schnell, *Nat. Commun.*, 2023, **14**, 934.
16 K. Banerjee-Ghosh, O. B. Dor, F. Tassinari, E. Capua, S. Yochelis, A. Capua, S. H. Yang, S. S. Parkin, S. Sarkar, L. Kronik, L. T. Baczewski, R. Naaman and Y. Paltiel, *Science*, 2018, **360**, 1331–1334.
17 A. Yachmenev, J. Onvlee, E. Zak, A. Owens and J. Küpper, *Phys. Rev. Lett.*, 2019, **123**, 243202.
18 E. G. Marklund, T. Ekeberg, M. Moog, J. L. P. Benesch and C. Carleman, *J. Phys. Chem. Lett.*, 2017, **8**, 4540–4544.
19 A. Sinelnikova, T. Mandl, H. Agelii, O. Grånäs, E. G. Marklund, C. Caleman and E. De Santis, *Biophys. J.*, 2021, **120**, 3709–3717.
20 Y. Kurosaki, K. Yokoyama and Y. Ohtsuki, *AIP Conf. Proc.*, 2022, **2611**, 20010.
21 C. Saribal, A. Owens, A. Yachmenev and J. Küpper, *J. Chem. Phys.*, 2021, **154**, 71101.
22 H. J. Loesch and A. Remscheid, *J. Chem. Phys.*, 1990, **93**, 4779.
23 J. M. Rost, J. C. Griffin, B. Friedrich and D. R. Herschbach, *Phys. Rev. Lett.*, 1990, **68**, 1299–1302.
24 B. Friedrich and D. R. Herschbach, *J. Chem. Phys.*, 1999, **111**, 6157.
25 I. Nevo, L. Holmegaard, J. H. Nielsen, J. L. Hansen, H. Stapelfeldt, F. Filsinger, G. Meijer and J. Küpper, *Phys. Chem. Chem. Phys.*, 2009, **11**, 9912.

26 J. S. Kienitz, K. Długołecki, S. Trippel and J. Küpper, *J. Chem. Phys.*, 2017, **147**, 024304.
27 J. Bulthuis, J. Miller and H. J. Loesch, *J. Phys. Chem. A*, 1997, **101**, 7684–7690.
28 D. J. Tannor, R. Kosloff and S. A. Rice, *J. Chem. Phys.*, 1986, **85**, 5805–5820.
29 C. Brif, R. Chakrabarti and H. Rabitz, *New J. Phys.*, 2010, **12**, 075008.
30 C. P. Koch, U. Boscain, T. Calarco, G. Dirr, S. Filipp, S. J. Glaser, R. Kosloff, S. Montangero, T. Schulte-Herbrüggen, D. Sugny and F. K. Wilhelm, *EPJ Quantum Technol.*, 2022, **9**, 19.
31 J. Werschnik and E. K. U. Gross, *J. Phys. B: At., Mol. Opt. Phys.*, 2007, **40**, R175–R211.
32 C. P. Koch, *J. Phys.: Condens. Matter*, 2016, **28**, 213001.
33 R. Kosloff, S. A. Rice, P. Gaspard, S. Tersigni and D. J. Tannor, *Chem. Phys.*, 1989, **139**, 201–220.
34 Q. Ansel, J. Fischer, D. Sugny and B. Bellomo, *Phys. Rev. A*, 2022, **106**, 043702.
35 L. H. Delgado-Granados, C. A. Arango and J. G. López, *Phys. Chem. Chem. Phys.*, 2022, **24**, 21250–21260.
36 N. Khaneja, T. Reiss, C. Kehlet, T. Schulte-Herbrüggen and S. J. Glaser, *J. Magn. Reson.*, 2005, **172**, 296–305.
37 V. F. Krotov and I. N. Feldmann, *Eng. Cybern.*, 1983, **21**, 123–130.
38 D. J. Tannor, V. Kazakov and V. Orlov, in *Time-Dependent Quantum Molecular Dynamics*, ed. J. Broeckhove and L. Lathouwers, Springer US, Boston, MA, 1992, pp. 347–360.
39 E. Dmitriev and N. Bukharskii, *Photonics*, 2023, **10**, 803.
40 L. H. Coudert, *J. Chem. Phys.*, 2017, **146**, 024303.
41 A. Beer, R. Damari, Y. Chen and S. Fleischer, *J. Phys. Chem. A*, 2022, **126**, 3732–3738.
42 R. Damari, A. Beer, D. Rosenberg and S. Fleischer, *Opt. Express*, 2022, **30**, 44464–44471.
43 L. H. Coudert, *J. Chem. Phys.*, 2018, **148**, 094306.
44 A. Pelzer, S. Ramakrishna and T. Seideman, *J. Chem. Phys.*, 2008, **129**, 134301.
45 J. Salomon, C. M. Dion and G. Turinici, *J. Chem. Phys.*, 2005, **123**, 144310.
46 J. J. Omiste, M. Gärttner, P. Schmelcher, R. González-Férez, L. Holmegaard, J. H. Nielsen, H. Stapelfeldt and J. Küpper, *Phys. Chem. Chem. Phys.*, 2011, **13**, 18815–18824.
47 W. Kong and J. Bulthuis, *J. Phys. Chem. A*, 2000, **104**, 1055–1063.
48 R. N. Zare, *Angular Momentum: Understanding Spatial Aspects in Chemistry and Physics*, John Wiley and Sons, New York, 1988.
49 Y. Ohtsuki, G. Turinici and H. Rabitz, *J. Chem. Phys.*, 2004, **120**, 5509–5517.
50 T. J. Park and J. C. Light, *J. Chem. Phys.*, 1986, **85**, 5870–5876.
51 J. L. Hansen, J. J. Omiste, J. H. Nielsen, D. Pentlehner, J. Küpper, R. González-Férez and H. Stapelfeldt, *J. Chem. Phys.*, 2013, **139**, 234313.
52 J. J. Omiste, R. González-Férez and P. Schmelcher, *J. Chem. Phys.*, 2011, **135**, 064310.
53 L. V. Thesing, J. Küpper and R. González-Férez, *J. Chem. Phys.*, 2017, **146**, 244304.
54 M. H. Goerz, D. Basilewitsch, F. Gago-Encinas, M. G. Krauss, K. P. Horn, D. M. Reich and C. P. Koch, *SciPost Phys.*, 2019, **7**, 80.
55 M. Leibscher, E. Pozzoli, A. Blech, M. Sigalotti, U. Boscain and C. P. Koch, *arXiv*, preprint, 2023, arXiv:2310.11570, DOI: **10.48550/arXiv.2310.11570**.
56 T. Eriksson, S. Björkman, B. Roth, Å. Fyge and P. Höuglund, *Chirality*, 1995, **7**, 44–52.

